Topological Analysis of Trabecular Bone MR Images

Bryon R. Gomberg, Punam K. Saha, Hee Kwon Song, Scott N. Hwang and Felix W. Wehrli

Abstract-- **Recently, imaging techniques have become available which permit non-destructive analysis of the three-dimensional (3D) architecture of trabecular bone (TB), which forms a network of interconnected plates and rods. Most osteoporotic fractures occur at locations rich in TB, which has spurred the search for architectural parameters as determinants of bone strength. In this paper, we present a new approach to quantitative characterization of the 3D micro-architecture of TB, based on digital topology. The method classifies each voxel of the 3D structure based on the connectivity information of neighboring voxels. Following conversion of the 3D digital image to a skeletonized surface representation containing only one- and two-dimensional structures, each voxel is classified as a curve, surface, or junction. The method has been validated by means of synthesized images and has subsequently been applied to TB images from the human wrist. The topological parameters were found to predict Young's modulus for uniaxial loading; specifically, the surface-to-curve ratio was found to be the single strongest predictor of Young's modulus ($r^2 = 0.69$). Finally, the method has been applied to TB images from a group of patients showing very large variations in topological parameters that parallel much smaller changes in bone volume fraction.**

Index terms-- **Magnetic resonance imaging (MRI), topology, trabecular bone, structure.**

I. INTRODUCTION

Trabecular bone consists of a lattice of interconnected plates and rods that confer mechanical strength to the skeleton at minimum weight [1]. There is growing evidence that besides the volume fraction of the bone (often quantified in terms of bone density) the three-dimensional arrangement of the trabecular network is a major determinant of elastic modulus [2] and ultimate strength. The small size of the structural elements (trabeculae) and the anatomic location of trabecular bone (e.g. vertebrae) make it difficult to image *in vivo* with sufficient resolution. Recently, peripheral computed tomography [3, 4] and magnetic resonance (MR) micro-imaging have been able to resolve individual trabeculae at peripheral skeletal locations, such as the wrist [5-7], and have been shown useful in deriving *in vivo* trabecular structural quantities. In general, characterization of the strength of trabecular lattices from three-dimensional (3D) images can be divided into three major categories: material, scale and topology [8]. Material properties describe the bone material, scale properties describe the size and thickness of the trabecular

B. R. Gomberg is with the Department of Bioengineering, 3320 Smith Walk, University of Pennsylvania, Philadelphia, PA 19104

P. K. Saha is with the Medical Image Processing Group, Department of Radiology, 423 Guardian Drive, University of Pennsylvania Health System, Philadelphia, PA 19104

H. K. Song, S. N. Hwang, and F. W. Wehrli (corresponding author) are with the Laboratory for Structural NMR Imaging, Department of Radiology, 3400 Spruce Street, University of Pennsylvania Health System, Philadelphia, PA 19104 (e-mail: wehrli@oasis.rad.upenn.edu)

elements, and the topological properties describe the arrangement of the bone material in the network. Osteoporosis is characterized as a disorder resulting from bone erosion assuming no change in the bone's intrinsic material properties [9]. The most common diagnostic screening method for osteoporosis is based on dual-energy X-ray absorptiometry (DEXA) [10] that measures integral bone mineral density (BMD). This method does not distinguish between trabecular and cortical bone and ignores the role of structure as a contributor to mechanical competence [9]. The present study is concerned with trabecular bone topology, which characterizes the microarchitectural arrangement of the bone network.

Topology is the branch of mathematics concerned with the geometric properties of deformable objects (that are invariant in scale, rotation and translation) [11]. For example, topological criteria allow us to determine whether a particular point in the network is part of a surface, curve, or junction. To illustrate the difference between topology and scale, consider a trabecular bone network that undergoes slight uniform thickening. Topologically, the network remains unaltered but the scale properties have changed, which will result in changes to the mechanical properties. Conversely, given two isotropic networks with identical bone volume fraction (BVF), one with more plate-like trabecular bone is assumed stronger than one that has trabeculae that are more rod-like. In this case, the two networks differ in topology.

In recent years the debate on the role of trabecular bone architecture in determining bone strength has intensified. There is some consensus that variations in the 3D arrangement [12] and the nature of the trabeculae (e.g. plate-like versus rod-like) [13] can help explain the variation in elastic moduli and ultimate strength of trabecular bone networks that is unaccounted for by density alone [14, 15]. Previous attempts to predict strength based on two-dimensional (2D) architectural measures characterizing the trabecular bone network are numerous [3, 16-20], yet it is well known that connectivity analysis of 2D sections does not accurately define the 3D structures found in trabecular bone networks [21]. For example, what would appear to be a rod in a 2D section may be a cross-section of a plate-like structure in the 3D network, or even a junction between two plates. A 3D analysis is thus essential to unambiguously establish the topology of the trabecular architecture. [22]. Feldkamp *et al.* [23] were among the first to use 3D topological measures to describe trabecular lattices from micro-CT images by estimating the global network connectivity using the Euler characteristic. This method is limited by its failure to provide information on the spatial distribution of connectivity and it cannot distinguish between perforation of trabecular bone plates and disconnection of rods [24, 25].

Digital topological analysis classifies each voxel in a 3D structure based on the connectivity information of the neighboring voxels [26]. The process begins with converting the 3D network to a skeletonized surface representation, which consists of only one- and two-dimensional structures (i.e. curves

and surfaces). Throughout this work, we will use rods and plates to refer to the gray scale image representations of trabecular structures while curves and surfaces will refer to their surface skeleton representations. Each image voxel is then classified in a three-step approach as belonging to a curve, surface, or junction. The method was validated with synthetic images and applied to a range of MR images of human trabecular bone from the distal radius.

II. Topological Theory*

The basis of digital topology relies on calculating the number of objects, tunnels, and cavities in the immediate neighborhood of each bone voxel. Here, we briefly describe the mathematical basis of digital topological analysis in the context of trabecular bone images. Digital topology deals with binary images, here defined as 3D matrices of voxels whose positions are represented by a vector of Cartesian coordinates, $x = (x_1, x_2, x_3)$, and whose voxels can have only one of two values, bone or marrow. Such an image might be produced by binarizing a gray-scale intensity image, such as an image where the intensities represent the BVF occupied by each voxel. Two voxels x and y are called 6-*adjacent* if $|x-y| = 1$ (face adjacent only); 18-*adjacent* if $|x-y| \leq \sqrt{2}$ (face and edge adjacent); and 26-*adjacent* if $|x-y| \leq \sqrt{3}$ (face, edge and corner adjacent). It may be noted that higher order adjacencies (i.e. 26-*adjacency*) include the lower order adjacencies (i.e. 6- or 18-*adjacency*). When considering binary images, the voxels are separated into two sets, one for bone (foreground) and one for marrow (background). Let S be a set of bone voxels, such as all the bone voxels in a binary image. An r-*path* (where r can be 6, 18 or 26) between two voxels $p, q \in S$ means a sequence of voxels p_0, $p_1, \ldots, p_n$ ($p = p_0$ and $q = p_n$) in S such that p_i is r-*adjacent* to p_{i+1}, $0 \leq i < n$. Two voxels $p, q \in S$ are r-*connected* in S if there exists an r-*path* from p to q in S. An r-*object* of S is a maximal subset of S where each pair of voxels is r-*connected*.

To satisfy the Jordan curve theorem, bone objects are defined as 26-*objects* of bone voxels (i.e. 26-*connected*) and marrow objects (background) are 6-*objects* of marrow voxels [27, 28]. In general, cavities are marrow objects surrounded by bone. Since physiology tells us that the entire marrow space in trabecular bone is connected, no such cavities exist in reality. However, to determine the local neighborhood connectivity, the central bone voxel is considered a marrow voxel (described below) which, technically, could result in a single voxel cavity. For example, when three straight, orthogonal, 6-*connected* bone curves intersect, the voxel at the intersection forms a single-voxel cavity because all it's 6-*neighbors* are bone voxels. While a cavity is relatively easy to define, the concept of a tunnel in digital space is slightly more complicated. The simplest illustration of a tunnel in continuos space is the loop formed by a coffee mug's handle. In fact, the topological term "handle" is directly related to tunnels. Topologically, a handle

---

* Glossary of mathematical symbols:
$\in$ element of
$\cap$ intersection of
$\exists$ there exists
$|x|$ Euclidean norm of x

is an object that can be elastically deformed to a simple, closed curve. It is thus obvious that opening a handle results in the loss of the tunnel. The number of tunnels in most objects can be counted by recursively reducing that object's handles. The number of objects, tunnels and cavities represent the 0th, 1st and 2nd Betti numbers, respectively.

For any bone voxel p, $M(p)$ denotes the set of 27 voxels in the 3x3x3 neighborhood of p (including the central voxel p) and $N^*(p)$ denotes the set of 26 voxels in the 3x3x3 neighborhood of p (excluding p, i.e. p is considered marrow). Since $M(p)$ always contains exactly one simply connected bone object without cavities [29], the topological properties of $M(p)$ are invariant and $N^*(p)$ must be used to characterize the local topology. A set of voxels, S, is called simply connected if it is connected and doesn't contain a tunnel. Let $\vartheta(p)$, $\gamma(p)$ and $u(p)$ denote the number of objects, tunnels and cavities, respectively, in the bone structure of $N^*(p)$. We call $\vartheta(p)$, $\gamma(p)$ and $u(p)$ local topological parameters of p. For convenience in counting tunnels in $N^*(p)$, let $X(p)$ and $Y(p)$ be the sets of 6- and 18-adjacent marrow voxels to p, respectively. It may be noted that a marrow object in $Y(p)$ will be 6-*adjacent* to p, if it contains a voxel that is 6-*adjacent* to p (i.e. intersects $X(p)$). The following two theorems, discussed in detail by Saha *et al.* [30], provide a computational definition of $\gamma(p)$ and $u(p)$ in the bone structure of $N^*(p)$:

Theorem 1: *The number of cavities, $\delta(p)$, in $N^*(p)$, is one when all the 6-neighbors of* p *are bone voxels and zero otherwise.*

Theorem 2: *If* X(p) *is non-empty, the number of tunnels, $\eta(p)$, is one less than the number of marrow objects in the intersection of* X(p) *and* Y(p)*, or zero otherwise.*

Using these two theorems, we can compute the number of tunnels and cavities in N*(p), while the number of objects can be computed using standard algorithms [31]. These local topological parameters are the basis for topological classification described below.

III. Methods

A. Topological Classification and Analysis

The topological classes determined by classical digital topology are as follows (Figure **1**): isolated voxels (*I*-type), curve interiors (*C*-type), curve edges (*CE*-type), curve-curve junctions (*CC*-type), surface interiors (*S*-type), surface edges (*SE*-type), surface-surface junctions (*SS*-type), and surface-curve junctions (*SC*-type). To these classes, we have introduced the concept of profile elements (*P*-type) described below.

After the number of objects, tunnels and cavities have been determined for each voxel ($\vartheta(p)$, $\gamma(p)$ and $u(p)$) in a skeletonized surface representation of the trabecular network, topological classification proceeds in three steps. This approach makes the method more straightforward to understand and efficient to implement. In addition, the three-step approach ensures classification in some cases where the local topological parameters of a single voxel cannot uniquely determine the topological class [32]. The unique classification of p can be determined by looking at the parameters of the voxels neighboring p. Step (a) is achieved by resorting to Table 1, which determines only a partial topological classification. Specifically, T_1, T_3, and T_4 give unique initial voxel classifications while T_2, T_5, T_6, T_7, and T_8 give two or more initial voxel classifications. During step (b) the 26-

neighborhood of any voxel not uniquely classified by Table 1 is examined and Table 2 used for initial classification. The most elaborate of the three steps, step (c), detects profile elements and makes possible corrections at surface junctions.

Profiles were introduced after digital topological analysis of *in vivo* trabecular microimages. Partial volume mixing (voxel intensity averaging) could result in trabeculae being represented by a double row of voxels in the surface skeleton representation. Step (b) would classify these voxels as SE-type, but since these ribbon-like structures are better thought of as curves, we have introduced profiles, which is any *SE*-type voxel, *p*, with no neighboring *S*-type, *SC*-type or *SS*-type voxels. This definition is used in step (c) to determine the profile element (P-type) voxels in the image. To conclude step (c), we solve the problem of extension of surface-surface junctions (*SS*-lines) and correct unidentified surface-curve junction voxels, described in detail elsewhere [26, 32]. Following are the algorithms used for these determinations.

Let S_{SE} denote the set of all *SE*-type voxels in the surface representation. Let *p* be an end voxel of an *SS*-line. Note, an end voxel of an *SS*-line has at most one 26-*adjacent SS*-type voxel. So the single *SS*-type voxel in $N^*(p)$ will be denoted p_{SS}, and let Q_S denote the set of all *S*-type voxels in $N^*(p)$.

Algorithm 1:

FOR every *SE*-type voxel $q \in N^*(p) - N^*(p_{SS})$:

    IF (number_of_26-objects($S_{SE} \cap N^*(q)$) > 2) OR

        (number_of_tunnels($S_{SE} \cap N^*(q)$) > 0)

    THEN flag *q*;

    ELSE IF (number_of_26-objects($S_{SE} \cap N^*(q)$) = 1)

        AND ($\exists r \in Q_S \cap N^*(q) - N^*(p_{SS})$ such that

        $|q - r| < |q - p|$)

    THEN flag one of the nearest *r* to *q*

All flagged voxels are reclassified as *SS*-type voxels.

When a curve meets a surface, there will be a surface-curve junction in between them. After the second classification step, some of these surface-curve junctions will not be detected. To correct this we must look at surface voxels with neighboring curve voxels and make corrections as needed. The algorithm is as follows: Let *p* be a *C*-type or *CC*-type voxel and let *Q* be the set of *S*-type, *SC*-type and *SS*-type voxels in $N^*(p)$. Let O_1, O_2, … O_n be the 26-objects in *Q*. If O_i has no *SC*-type or *SS*-type voxels, the nearest voxel to *p* in O_i is reclassified as a *SC*-type voxel.

Once the topological classification has been completed, the results need to be further evaluated to account for volume of interest (VOI) edge artifacts. Edge artifacts result from the method identifying edges in the trabecular structure caused by the VOI boundaries. These artificial edges are further modified by of the skeletonization process. During each iteration of the skeletonization process, the edges propagate one voxel layer into the structure at most. Therefore, for *n* skeletonization iterations, the VOI used for voxel classification counting would need to be eroded using a mask size of 2*n*+1. Finally, to compare the voxel counts from different subjects, the classification counts need to

be normalized to the VOI volume. The final classification density can be calculated by a straightforward division of the classification count by the total VOI voxel count.

B. Images

To validate and demonstrate the method, the topological method was applied to three types of data: synthetic, trabecular bone specimen, and *in vivo* images. Synthetically generated data were intended to demonstrate the accuracy and reliability of the method. The image data sets from specimens of the human distal radius, previously studied by means of spatial auto-correlation analysis [33], were re-examined to assess the potential of topological analysis as a means to predict the trabecular networks' mechanical properties. Finally, evidence is provided that the method is applicable to trabecular bone images acquired *in vivo* from patients of varying skeletal status.

Since current *in vivo* MRI resolution is on the order of the trabecular thickness, accuracy of the topological parameters as a function of structure resolution is of particular interest. To create synthetic images of rod-like and plate-like structures that mimic the variations seen *in vivo*, cubic spline curves and surfaces (IDL, Research Systems, Inc., Boulder, CO) were fitted through regular grid points with random variations in position (Figure 2). Partial volume mixing was mimicked and Rician noise [34] of similar magnitude to *in vivo* images (signal-to-noise ratio ≈ 15) was added. Three independently generated synthetic images were analyzed for absolute accuracy by calculating the ratio of average measured voxel counts to the true voxel counts known from the generation of the synthetic images.

The cadaveric specimen images (n=22, 8 females, 14 males) had a voxel size of 78x78x78 μm^3. The ages and elastic moduli (in the axial direction) for these specimens ranged from 53 to 87 years old and 104 to 712 MPa, respectively. These images displayed a wide range of morphologies from predominantly rod-like to predominantly plate-like architecture. The specific question addressed was whether topological parameters would be able to predict Young's modulus for uniaxial loading. Details on the pulse sequence and imaging methods can be found in [33].

In vivo images were acquired as part of an ongoing clinical study to evaluate the architectural changes that occur during osteoporotic bone loss. These images of the distal radius were acquired on a clinical magnetic resonance scanner (1.5 T General Electric Signa™, Milwaukee, WI). A custom-designed 3D spin-echo pulse sequence [35] (radio-frequency pulse flip angle = 140°, TR = 80 msec, TE = 9.7 msec, 512x256x32 matrix size) was used with a home-built transmit-receive RF coil encompassing the distal end of the forearm. For each subject 32 contiguous images were acquired at 137x137 μm^2 in-plane resolution and 350μm slice thickness. In addition, the pulse sequence was equipped with navigator echoes to correct for translational motion of the wrist during scanning [36].

C. Preprocessing

All images were preprocessed by deshading and noise reduction using a histogram deconvolution method [37]. The resulting images represent the BVF at each voxel location. The VOI was manually outlined for each slice, and adjusted to exclude areas containing acquisition artifacts. For *in vivo* images, resolution

was enhanced using a subvoxel classification technique similar to the one described by Wu *et al.* [38] resulting in a final voxel size of $68 \times 68 \times 88 \mu m^3$. In this manner, an in-slice and across-slice continuity of the trabecular network was achieved, which aided the preservation of topology during the skeletonization procedure.

D. Thresholding and Skeletonization

As pointed out previously, topological parameters are derived from a surface representation of a binarized trabecular bone network. This means that all volume objects must be reduced to 1D or 2D structures, and there can be no bulk elements present in the digital image, which is accomplished by thresholding and skeletonizing. To determine the optimal threshold for binarization of the images, BVF thresholds from 0.01 to 0.99 were applied to the BVF images from five subjects of varying skeletal status as determined by DEXA BMD of the lumbar spine. These binarized images were thinned and the number of voxels in the surface skeleton representation counted. The averaged consecutive change in total skeleton voxel counts versus BVF threshold for all subjects reveals a local minimum at 0.25-0.40 BVF threshold (Figure 3). In this region, the skeleton structure changes minimally as a function of threshold, and therefore, a constant BVF threshold of 0.25 was used for all images. After thresholding, images were skeletonized using a recently published algorithm [39] because of its robustness to noise and rotation.

E. Prediction of Young's Modulus

Topological analysis determines the local connectivity properties of each skeletonized surface voxel. These properties were used to ascertain relationships with trabecular network competence of the bone specimens as represented by Young's modulus (YM) using regression analysis (JMP-IN, SAS Institute Inc., Cary, NC). Toward this goal Young's modulus data obtained in prior work on human wrist specimens were re-examined. The experiments are detailed in ref. [33]. In brief, YM was derived from stress-strain curves by uniaxial compression testing of cylindrical trabecular bone samples (9mm diameter and length) drilled parallel to the long axis of the bone from the ultra-distal radius of 13 cadavers [33]. Besides being considered individually, parameter densities were grouped by major topological category (isolated, curve, surface and junction) and averaged for the complete intra-cortical region. Two multi-parameter indices were calculated that we hypothesize should correlate with erosion status and hence strength: the surface-to-curve ratio and the topological erosion index. Using a surface-profile-curve erosion cascade model, an erosion index was defined as the ratio of all topological parameters expected to increase with erosion (C-type, CE-type, SE-type, PE-type, and CC-type) to all those that are expected to decrease by erosion (S-type and SS-type). Single-parameter linear and polynomial models were examined for all parameters to predict YM. Finally, linear combinations of the most promising topological parameters were evaluated as well.

F. Visualization

"Virtual bone biopsies" were generated for displaying projections of cylindrical cores extracted mathematically from the *in vivo* cancellous bone volumes. A longitudinal cylindrical VOI mask was automatically generated (diameter of 5.5 mm) through all slices containing bone. This VOI was positioned concentrically with the center of mass of the cancellous volume. Bone voxels were extracted from the BVF maps using a 0.25 threshold. To eliminate artifactual bone "fragments" left in the VOI, small and disconnected elements of bone were removed using 3D region growing based object analysis. To preserve large bone structures that might happen to be disconnected in the VOI, only objects comprising greater than 5% of the total VOI volume were retained for visualization. Median filtering was performed on the images to smooth the bone marrow interfaces and produce the best visual results. The "biopsies" were visualized using depth-queued nearest voxel projection (IDL, Research Systems, Inc. Boulder, CO).

IV. RESULTS AND DISCUSSION

Analysis of the synthetic images shows that for rod-like structures (i.e. curves) of greater than 0.9 voxel diameter the topological method has an absolute accuracy of 97% (Table 3). However, at lower structural resolutions, accuracy decreases rapidly. The increase in classification errors at lower resolutions can be explained by partial volume mixing of low BVF voxels. Since a rod can intersect between one and four voxels within each slice, rods of 0.6 and 0.7 diameters would result in maximum voxel BVFs ranging from 0.07 to 0.28 and 0.095 to 0.38, respectively. Recalling that the empirically determined BVF threshold for binarization was 0.25, one would expect that at low rod diameters many of the low BVF voxels would disappear. At greater rod diameters, BVF increases sufficiently for more elements to survive after thresholding, resulting in increased classification accuracy. The reproducibility for rods was estimated at 0.999 (p<0.0001) as determined by the intraclass correlation coefficient (ICC) [40].

For plates (surfaces), the absolute accuracy was greater than 98% for all plate thicknesses tested (Table 3), with an ICC for surface counts of 0.99 (p<0.0001). This result is consistent with the findings for the synthetic rod images - the extent of partial volume mixing is key in determining the structural elements that will survive the skeletonization. At a plate thickness of 0.6, the minimum BVF at any plate location will be 0.3 (when the plate is equally distributed across two voxels). Since the range of trabecular sizes in normal human bone is 100-150 μm, the choice of 0.25 as the BVF threshold and an *in vivo* resolution of $137 \times 137 \ \mu m^2$ should include most plate-like trabeculae of normal thickness. In osteoporosis, the trabecular thickness may be as low as 50 μm, in which case a voxel size of 50-100 μm may be needed to achieve accurate quantitative results from trabecular structures, as determined by micro-CT [41]. To achieve a pixel size of $100 \times 100 \ \mu m^2$, for example, would require a gain in signal-to-noise ratio of a factor 2 relative to our current in vivo resolution ($137 \times 137 \ \mu m^2$), which is achievable by imaging at higher magnetic field strength. Nevertheless, the results on synthetic image data suggest that most plate and rod voxels can accurately be identified at the present resolution. The accuracy of topological classification is illustrated in a small region of an *ex-vivo* surface skeleton image, displayed as a voxel projection in Figure 4, clearly showing the correct classification of surface and curve structures.

To evaluate whether topological parameters are predictive of YM, linear and polynomial models were tested. Table 4 shows

single-parameter linear regression results, from which it is evident that topological parameters compare favorably with BVF, some even suggesting stronger association with YM. A statistical test to determine whether the difference in the correlation coefficients was significant did not show this to be the case, presumably due to lack of sufficient power (low number of samples, n=22). The erosion index was found to be the strongest single linear predictor of YM ($r^2 = 0.67$; p<0.0001). The most predictive of all two-parameter, two-term linear models was the combination of 1/Snorm and 1/Cnorm ($r^2 = 0.79$; p<0.0001). In the previous study involving the same image and biomechanical data, Hwang *et al.* [33] found that two auto-correlation parameters alone could predict 91% of the variation in YM when they were combined in a complex non-linear, multiple-term, multiple-interaction model. However, auto-correlation parameters are measures of both structure and fabric, or orientation, of the trabecular lattice, and thus include important information not available directly using topological analysis. Fabric parameters could be derived from the local topological information by directly assessing the orientation at each voxel location, but this level of analysis is beyond the scope of the current study.

Our data emphasize the architectural contribution to cancellous bone competence. A number of investigators have reported improvements in modulus or strength prediction by incorporating measures of architecture into multi-variate models involving BVF or BMD [15, 42-44], showing that density and architectural parameters accounted for 60-90% of the variance in the modulus and ultimate strength. Gordon *et al.* [45] found in nine intact radii that measures of bone mineral density explained approximately 50% of the variability with load ($0.52 < r^2 < 0.57$, $p < 0.03$), while indices relating to the size of the marrow spaces explained an additional 25% to 30% of the variance. Oden *et al.* [46] reported that the mean intercept length in the specimen primary axis was strongly associated with failure stress ($r^2 = 0.85$, $p < 0.001$). BMD was also moderately associated with failure stress ($r^2 = 0.44$, $p = 0.004$). They found that using a stepwise linear multiple regression analysis, the strongest predictor of failure stress was a combination of BMD, specimen orientation angle, and mean intercept length ($r^2 = 0.91$).

The projection images of the in vitro data (Figure 5) are arranged in order of increasing visual "plate-likeness" and the topological parameters (Table 5) support this qualitative ordering. In the four specimens, the surface/curve ratio (a-d) was found to increase by more than an order of magnitude. Whereas there is an increase in surface density and decrease in curve density in the same order, each parameter varies far less than their ratio, which we postulate could serve as an indicator of trabecular bone erosion. The final measure, the erosion index, also emphasizes the qualitative trends of erosion (rod-versus plate-likeness) seen in these samples, changing from 1.5 in the most plate-like specimen (a) to 0.3 in the most rod-like one (d). It has been shown that erosion of trabeculae results in bone plates changing to rods, which eventually become disconnected [24, 25]. The transition phase between plates and rods is most likely a profile-like structure that is topologically unique.

In vivo analysis of trabecular bone exemplifies the potential merit of topological analysis with selected cases of subjects matched for BVF and spinal DEXA BMD T-scores, but having significantly different topologies. Figure 6 illustrates the differences in the distribution of bone in two BVF-matched subjects. Figure 7 shows data from two subjects with very different trabecular architectures and topological parameters (15-30%), yet nearly equal BVF and T-scores. Finally, in Figure 8, surface counts and surface/curve ratios are plotted versus BVF, indicating the expected correlation between the two parameters. It is interesting, however, to note the enhanced sensitivity of these parameters to relatively small variations in BVF. For example, the surface/curve ratio varies four-fold for a less than two-fold variation in BVF. These data corroborate the notion that the decrease in bone mass is accompanied by a conversion from trabecular plates to rods and the disappearance of rods due to inhomogeneous thinning [25].

V. CONCLUSIONS

In this work, we have introduced 3D digital topology as a new method to quantitatively assess trabecular bone networks. The method allows unique determination of the topological identity of each voxel as belonging to a curve, junction, or surface. A detailed evaluation shows that the algorithm is remarkably robust over a wide range of resolutions as long as image voxel size is sufficient to resolves the structures under investigation. Applications to 3D MR microimages of trabecular bone from the human distal radius indicate that the volume densities of parameters such as the surface-to-curve ratio are strong predictors of Young's modulus. Analysis of *in vivo* MR microimages from the human wrist indicate that topological parameter densities vary substantially among subjects though bone mineral densities do not distinguish them. Topological analysis is expected to give accurate *in vivo* results and characterize trabecular bone network integrity. Finally, the results displayed here show that topology is intrinsic to a particular network. Since each voxel is classified uniquely, this method produces localized connectivity information which, along with scale information (e.g. trabecular thickness) characterizes local network strength. Fractures are local failure phenomena and therefore topological classification might help predict both the risk and precise location of wrist fractures.

VI. ACKNOWLEDGMENTS

VII. REFERENCES

[1]   J. Wolff, Das Gesetz der Transformation der Knochen. Berlin: A. Hirschwald, 1892.

[2]   A. Odgaard, J. Kabel, B. van Rietbergen, M. Dalstra, and R. Huiskes, "Fabric and elastic principal directions of cancellous bone are closely related," Journal of Biomechanics, vol. 30, pp. 487-495, 1997.

[3]   C. L. Gordon, C. E. Webber, J. D. Adachi, and N. Christoforou, "In vivo assessment of trabecular bone structure at the distal radius from high-resolution computed tomography images," Physics in Medicine and Biology, vol. 41, pp. 495-508, 1996.

[4]   R. Muller, T. Hildebrand, H. J. Hauselmann, and P. Ruegsegger, "In vivo reproducibility of three-dimensional structural properties of noninvasive bone biopsies using 3D-pQCT," Journal of Bone and Mineral Research, vol. 11, pp. 1745-1750, 1996.

[5]   S. Majumdar, H. K. Genant, S. Grampp, D. C. Newitt, V.-H. Truong, J. C. Lin, and A. Mathur, "Correlation of trabecular bone structure with age, bone, mineral density, and osteoporotic status: in vivo studies in the distal radius using high-resolution magnetic resonance imaging," Journal of Bone and Mineral Research, vol. 12, pp. 111-118, 1997.

[6]   C. L. Gordon, C. E. Webber, N. Christoforou, and C. Nahmias, "In vivo assessment of trabecular bone structure at the distal radius from high-resolution magnetic resonance images," Med Phys, vol. 24, pp. 585-593, 1997.

[7]   F. W. Wehrli, S. N. Hwang, J. Ma, H. K. Song, J. C. Ford, and J. G. Haddad, "Cancellous bone volume and structure in the forearm: noninvasive assessment with MR microimaging and image processing [published erratum appears in Radiology 1998 Jun;207(3):833]," Radiology, vol. 206, pp. 347-357, 1998.

[8]   R. T. DeHoff, E. H. Aigeltinger, and K. R. Craig, "Experimental determination of the topological properties of three-dimensional microstructures," Journal of Microscopy, vol. 95, pp. 69-91, 1972.

[9]   WHO Techincal Report Series no. 843, "Assessment of fracture risk and its application to screening for postmenopausal osteoporosis," World Health Organization, Geneva 1994.

[10]   H. W. Wahner and I. Fogelman, The evaluation of osteoporosis: dual energy X-ray absorptiometry in clinical practice. Cambridge: University Press, 1994.

[11]   C. R. F. Maunder, Algebraic Topology. Cambridge, UK: Cambridge Univ. Press, 1980.

[12]   L. Mosekilde, "Age-related changes in vertebral trabecular bone architecture--assessed by a new method," Bone, vol. 9, pp. 247-50, 1988.

[13]   M. Morita, A. Ebihara, M. Itoman, and T. Sasada, "Progression of osteoporosis in cancellous bone depending on trabecular structure," Ann Biomed Eng, vol. 22, pp. 532-9, 1994.

[14]   M. J. Ciarelli, S. A. Goldstein, J. L. Kuhn, D. D. Cody, and M. B. Brown, "Evaluation of orthogonal mechanical properties and density of human trabecular bone from the major metaphyseal regions with materials testing and computed tomography," Journal of Orthopaedic Research, vol. 9, pp. 674-82, 1991.

[15]   R. W. Goulet, S. A. Goldstein, M. J. Ciarelli, J. L. Kuhn, M. B. Brown, and L. A. Feldkamp, "The relationship between the structural and orthogonal compressive properties of trabecular bone," Journal of Biomechanics, vol. 27, pp. 375-89, 1994.

[16]   A. M. Parfitt, "Stereologic Basis of Bone Histomorphometry: Theory of Quantitative Microscopy and Reconstruction of the Third Dimension," in Bone Histomorphometry: Techniques and Interpretation, R. R. Recker, Ed. Boca Raton, FL: CRC Press, 1981, pp. 53-87.

[17]   A. M. Parfitt, C. H. E. Mathews, A. R. Villanueva, M. Kleerekoper, B. Frame, and D. S. Rao, "Relationships between surface, volume, and thickness of iliac trabecular bone in aging and in osteoporosis. Implications for the microanatomic and cellular mechanisms of bone loss," Journal of Clinical Investigation, vol. 72, pp. 1396-409, 1983.

[18]   A. Vesterby, "Star volume of marrow space and trabeculae in iliac crest: sampling procedure and correlation to star volume of first lumbar vertebra," Bone, vol. 11, pp. 149-155, 1990.

[19]   M. Hahn, M. Vogel, M. Pompesius-Kempa, and G. Delling, "Trabecular bone pattern factor -- a new parameter for simple quantification of bone microarchitecture," Bone, vol. 13, pp. 327-330, 1992.

[20]   N. J. Garrahan, R. W. E. Mellish, and J. E. Compston, "A new method for the two-dimensional analysis of bone structure in human iliac crest biopsies.," Journal of Microscopy, vol. 142, pp. 341-349, 1986.

[21]   A. Odgaard and H. J. Gundersen, "Quantification of connectivity in cancellous bone, with special emphasis on 3-D reconstructions," Bone, vol. 14, pp. 173-82, 1993.

[22]   M. Wessels, R. P. Mason, P. P. Antich, J. E. Zerwekh, and C. Y. Pak, "Connectivity in human cancellous bone by three-dimensional magnetic resonance imaging," Medical Physics, vol. 24, pp. 1409-20, 1997.

[23]   L. A. Feldkamp, S. A. Goldstein, A. M. Parfitt, G. Jesion, and M. Kleerekoper, "The direct examination of three-dimensional bone architecture in vitro by computed tomography," Journal of Bone and Mineral Research, vol. 4, pp. 3-11, 1989.

[24]   M. Amling, M. Posl, H. Ritzel, M. Hahn, M. Vogel, V. J. Wening, and G. Delling, "Architecture and distribution of cancellous bone yield vertebral fracture clues. A histomorphometric analysis of the complete spinal column from 40 autopsy specimens," Arch Orthop Trauma Surg, vol. 115, pp. 262-9, 1996.

[25]   A. M. Parfitt, "Implications of architecture for the pathogenesis and prevention of vertebral fracture," Bone, vol. 13, pp. S41-47, 1992.

[26]   P. K. Saha and B. B. Chaudhuri, "3D digital topology under binary transformation with applications," Computer Vision and Image Understanding, vol. 63, pp. 418-429, 1996.

[27]   A. Rosenfeld, "Adjacency in Digital Pictures," Information and Control, vol. 26, pp. 24-33, 1974.

[28]   T. Y. Kong and A. Rosenfeld, "Digital Topology: Introduction and Survey," Computer Vision Graphics and Image Processing, vol. 48, pp. 357-393, 1989.

[29]   P. K. Saha and A. Rosenfeld, "Strongly Normal Sets of Convex Polygons or Polyhedra," Pattern Recognition Letters, vol. 19, pp. 1119-1124, 1998.

[30]   P. K. Saha and A. Rosenfeld, "Determining simplicity and computing topological change in strongly normals partial tilings of R^2 and R^3," Pattern Recognition, vol. in press.

[31]   J. K. Udupa and V. G. Ajjanagadde, "Boundary and Object Labelling in Three-Dimensional Images," Computer Vision Graphics and Image Processing, vol. 51, pp. 355-369, 1990.

[32]   P. K. Saha, B. R. Gomberg, and F. W. Wehrli, "Three-dimensional digital topological characterization of cancellous bone architecture," International Journal of Imaging Systems and Technology, in press.

[33]   S. N. Hwang, F. W. Wehrli, and J. L. Williams, "Probability-based structural parameters from 3D NMR images as predictors of trabecular bone strength," Med Phys, vol. 24, pp. 1255-1261, 1997.

[34]   H. Gudbjartsson and S. Patz, "The Rician distribution of noisy MRI data," Magnetic Resonance in Medicine, vol. 34, pp. 910-914, 1995.

[35]   J. Ma, F. W. Wehrli, and H. K. Song, "Fast 3D large-angle spin-echo imaging (3D FLASE)," Magnetic Resonance in Medicine, vol. 35, pp. 903-910, 1996.

[36]   H. K. Song and F. W. Wehrli, "In vivo micro-imaging using alternating navigator echoes with applications to cancellous bone structural analysis," Magn Reson Medicine, vol. 41, pp. 947-953, 1999.

[37] S. N. Hwang and F. W. Wehrli, "Estimating voxel volume fractions of trabecular bone on the basis of magnetic resonance images acquired in vivo," International Journal of Imaging Systems and Technology, vol. 10, pp. 186-198, 1999.

[38] Z. Wu, H. Chung, and F. W. Wehrli, "A Bayesian approach to subvoxel tissue classification in NMR microscopic images of trabecular bone," Magnetic Resonance in Medicine, vol. 31, pp. 302-308, 1994.

[39] P. K. Saha, B. B. Chaudhuri, and D. Duuta Majumder, "A new shape preserving parallel thinning algorithm for 3D digital images," Pattern Recognition, vol. 30, pp. 1939-1955, 1997.

[40] P. E. Shrout and J. L. Fleiss, "Intraclass correlations: Uses in assessing rater reliability," Psychological Bulletin, vol. 86, pp. 420-428, 1979.

[41] F. Peyrin, M. Salome, P. Cloetens, A. M. Laval-Jeantet, E. Ritman, and P. Ruegsegger, "Micro-CT examinations of trabecular bone samples at different resolutions: 14, 7 and 2 micron level," Technology & Health Care, vol. 6, pp. 391-401, 1998.

[42] R. S. Siffert, G. M. Luo, S. C. Cowin, and J. J. Kaufman, "Dynamic relationships of trabecular bone density, architecture, and strength in a computational model of osteopenia," Bone, vol. 18, pp. 197-206, 1996.

[43] S. A. Goldstein, R. Goulet, and D. McCubbrey, "Measurement and significance of three-dimensional architecture to the mechanical integrity of trabecular bone," Calcified Tissue International, vol. 53, pp. S127-133, 1993.

[44] R. Hodgskinson and J. D. Currey, "Effects of structural variation on Young's modulus of non-human cancellous bone," Proc Inst Mech Eng [H], vol. 204, pp. 43-52, 1990.

[45] C. L. Gordon, C. E. Webber, and P. S. Nicholson, "Relation between image-based assessment of distal radius trabecular structure and compressive strength," Canadian Association of Radiologists Journal, vol. 49, pp. 390-7, 1998.

[46] Z. M. Oden, D. M. Selvitelli, W. C. Hayes, and E. R. Myers, "The effect of trabecular structure on DXA-based predictions of bovine bone failure," Calcif Tissue Int, vol. 63, pp. 67-73, 1998.

VIII. TABLES AND FIGURES

Table 1: Topological type decision table for initial bone voxel topological analysis based on number of objects, tunnels and cavities among the voxel's 26-neighbors.

$\xi(p)$	$\eta(p)$	$\delta(p)$	Initial type	Possible final classification
0	0	0	T_1	I-type
1	0	0	T_2	SE- or CE-type
2	0	0	T_3	C-type
>2	0	0	T_4	CC-type
1	1	0	T_5	S- or CC-type
>1	≥1	0	T_6	SS- or SC- or CC-type
1	>1	0	T_7	SS- or SC- or CC-type
1	0	1	T_8	SS- or SC- or CC-type

Table 2: Voxel classification of the initial voxel types (Table 1) from the surface skeleton representation bone neighbors. Neighboring voxels are 26-adjacent bone voxels (bn = bone neighbor/s). This step resolves ambiguities from the initial type determination, but still requires refinement of some junction cases and determination of profile type voxels.

Initial Type	Neighborhood Analysis	Final Classification
T_2	Exactly one bn	CE-type
T_2	More than one bn	SE-type
T_5	All bn are T_3 or T_4	CC-type
T_5	Not all bn are T_3 or T_4	S-type
T_6	All bn are T_3 or T_4	CC-type
T_6	Some (not all) bn are T_3 or T_4	SC-type
T_6	No bnare T_3 or T_4	SS-type
T_7	All bn are T_3 or T_4	CC-type
T_7	Some (not all) bn are T_3 or T_4	SC-type
T_7	No bn are T_3 or T_4	SS-type
T_8	All bn are T_3 or T_4	CC-type
T_8	Some (not all) bn are T_3 or T_4	SC-type
T_8	No bn are T_3 or T_4	SS-type

Table 3: Results of synthetic image analysis showing absolute accuracy of the topological analysis method as a function of structural resolution. Curve diameter and surface thickness are relative to the voxel size.

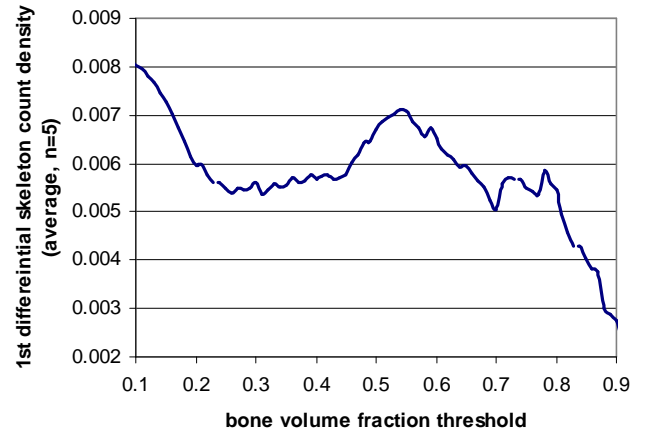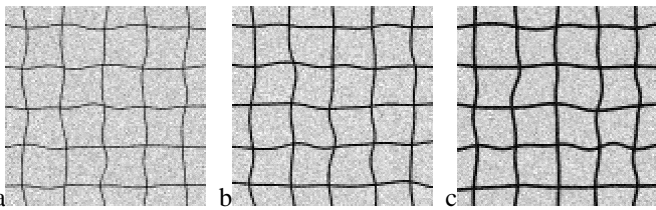| Curve diameter	Accuracy %	Stdev %	Surface thickness	Accuracy %	Stdev %
0.6	51.0	0.6	0.6	98.0	0.05
0.7	50.6	0.8	0.7	98.4	0.04
0.8	85.1	0.2	0.8	98.4	0.08
0.9	90.2	0.2	0.9	98.2	0.03
1	96.6	0.1	1	98.2	0.09
1.1	97.2	0.1	1.1	98.0	0.04
1.2	97.7	0.04	1.2	98.0	0.11
1.3	97.5	0.1	1.3	98.3	0.05
1.4	97.6	0.1	1.4	98.8	0.18
1.5	97.7	0.04	1.5	98.7	0.01
1.6	98.5	0.2	1.6	98.6	0.12

Table 4: Single parameter prediction of elastic modulus (n=22). All parameters are global for the complete volume of interest and have $p < 0.001$.

Parameter, type*	r^2	Correlation
Erosion index, topo	0.67	Negative
PEnorm, topo	0.66	Negative
surf/curv, topo	0.59	Positive
BVF, scale	0.57	Positive
Snorm, topo	0.51	Positive
Surf, topo	0.46	Positive

- * - Scale or topological (topo);

Table 5: Topological classification densities of images in Figure 5.

Sample	surface density	curve density	Skeleton density	Surface/ curve	Erosion Index
1	0.039	0.0112	0.054	3.5	1.46
2	0.059	0.0060	0.067	9.8	0.74
3	0.082	0.0052	0.092	15.7	0.60
4	0.103	0.0018	0.110	58.1	0.30
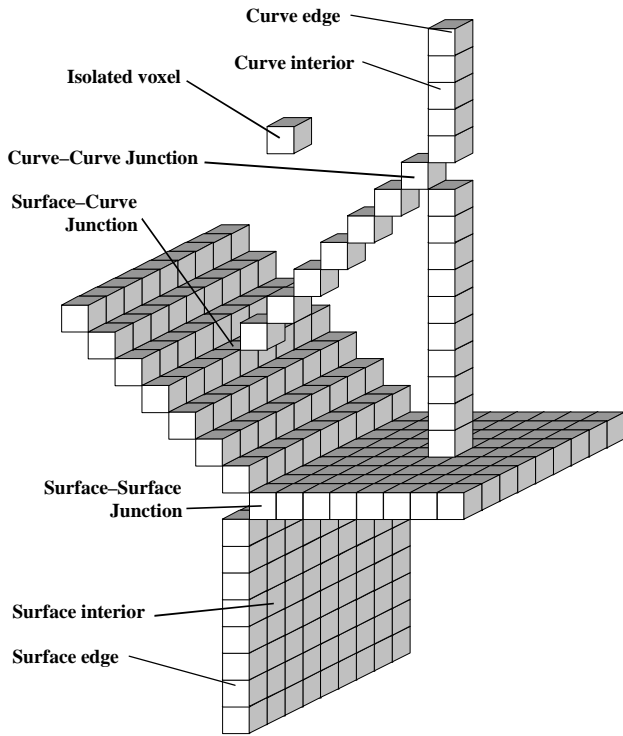
Figure 1: Illustration of topological classification of voxels in an idealized structure. Shown are examples of isolated (I-type), curve edge (CE-type), curve interiors (C-type), surface edge (SE-type), surface interiors (S-type), surface-surface junction (SS-type), surface-curve junction (SC-type), and curve-curve junction (CC-type).

Figure 2: Examples of synthetic images used to evaluate the absolute accuracy of topological analysis. The 3D dataset is filled with a 5x5x5 grid of "wavy" plates at varying voxel thicknesses. Pictured are 0.6 (a), 1.1 (b) and 1.6 (c) voxel thick plate arrays viewed edge-on.

Figure 3: First differential of skeleton voxel count (average count density of five subjects) showing a region of minimum change around 0.25 - 0.40 bone volume fraction. A bone volume fraction threshold of 0.25 allows preservation of the connectivity of the partial volume structure regime shown by this local minimum.
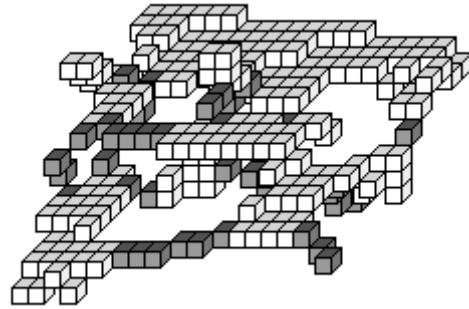
Figure 4: Voxel display of topological classification results in skeletonized trabecular bone showing surface and curve voxels (light and dark, respectively). The data represent a subregion of 10x20x20 voxels taken from an image obtained at $(78\mu m)^3$ voxel size.
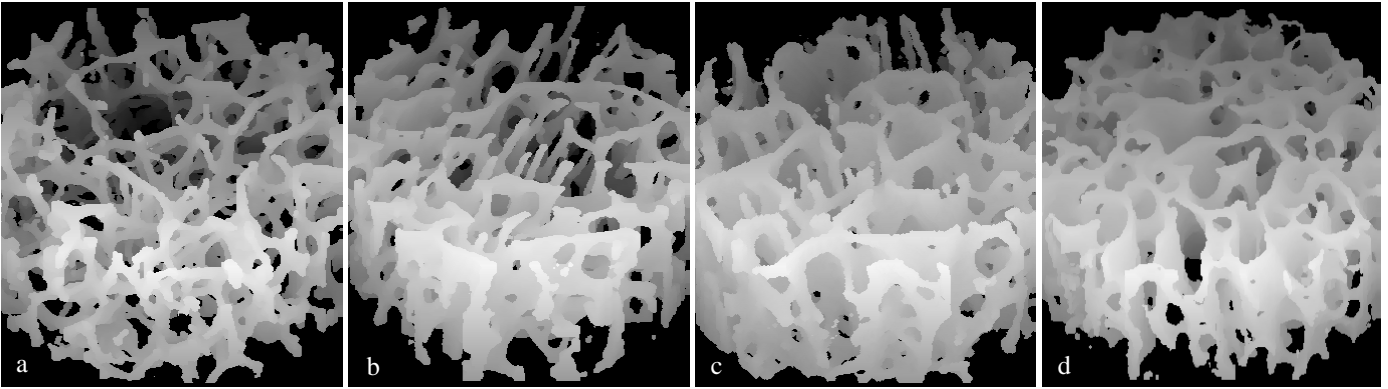
Figure 5: Qualitative examples of plate-like and rod-like networks: a) highly rod-like (74 yo female) b) medium rod-like (53 yo female) c) highly plate-like (68 yo female) d) very highly plate-like (60 yo male). Topological parameters (Table 5) support visual assessment of increasing plate-like morphology.
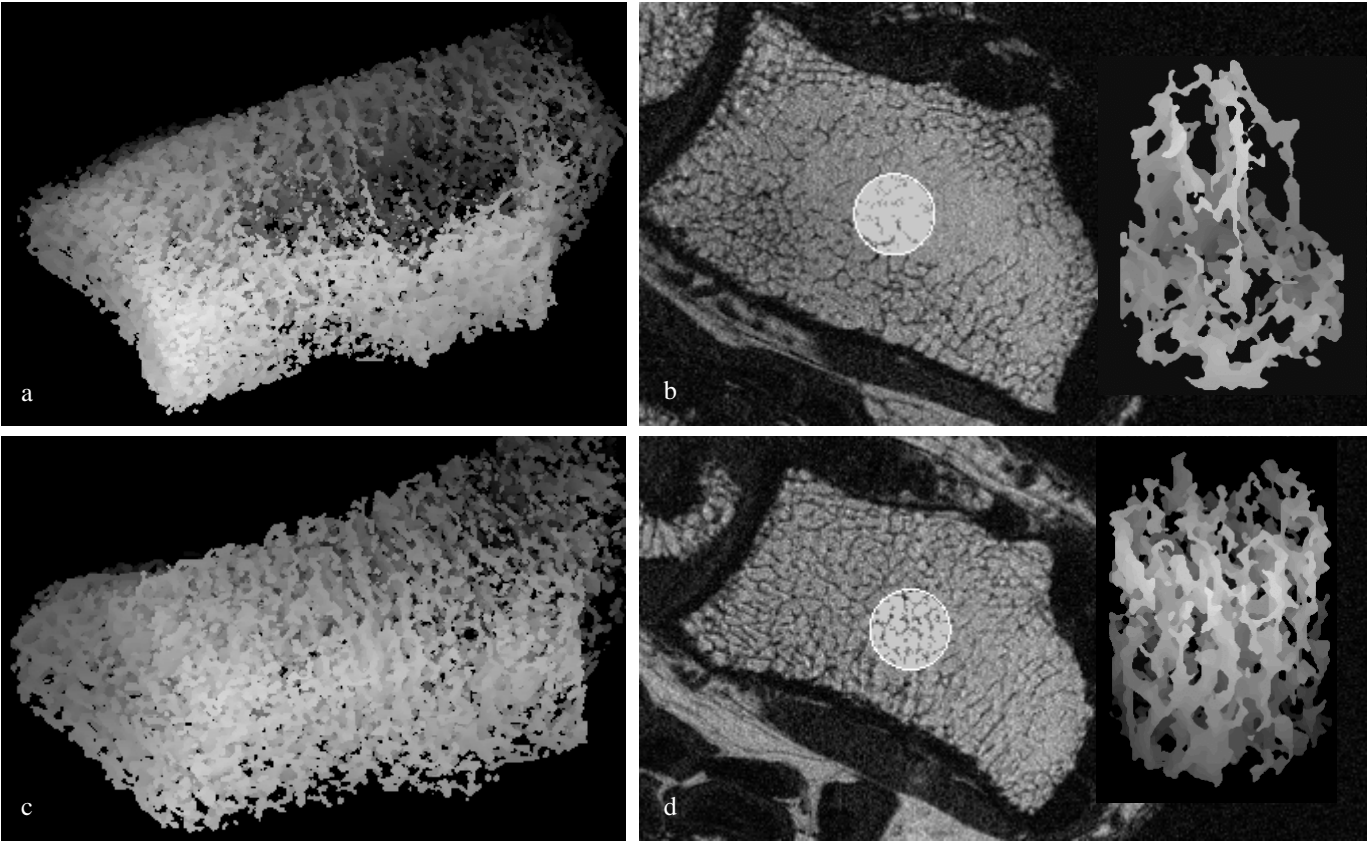

Figure 6: *In vivo* projection and transverse micro-images for two normal subjects (#1: a, b; #2: c, d) with equal bone volume fraction (0.118) and spinal DEXA BMD T-scores (L2-L4). Subject 1 shows dramatic central cancellous bone erosion not seen in subject 2. Topological parameters show subject #2 having an overall increased surface density (+9.6%) and a decreased profile density (-4.6%) over subject #1.
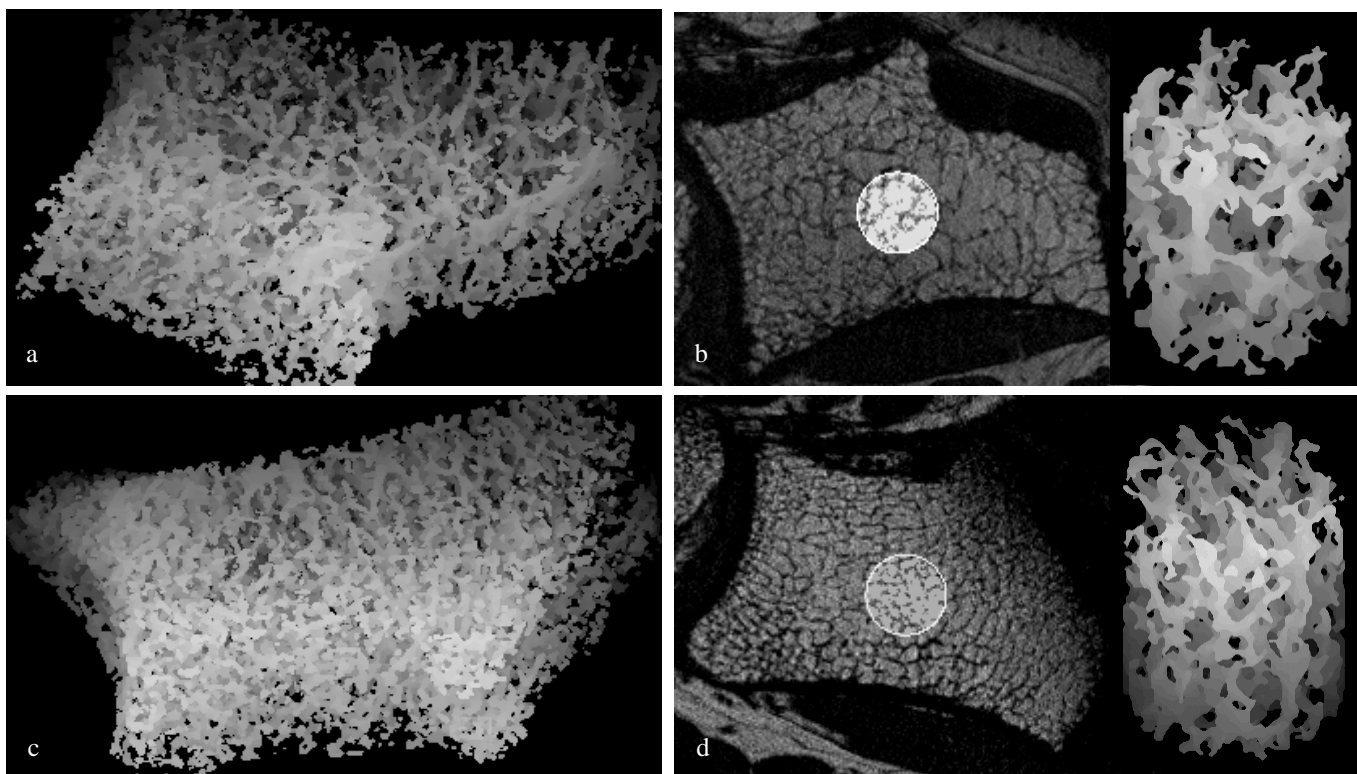
Figure 7: *In vivo* images for two osteoporotic subjects (#3: a, b; #4: c, d) with similar DEXA BMD T-scores (-3.6 and –3.76) and bone volume fraction (0.123 and 0.134), but with very different trabecular topologies. Topological parameters show subject #4 having a highly increased overall S-type density (+45%), an increased surface/curve ratio (+26%) and a decreased erosion index (-18%) over subject #3, all of which indicate a stronger trabecular network.
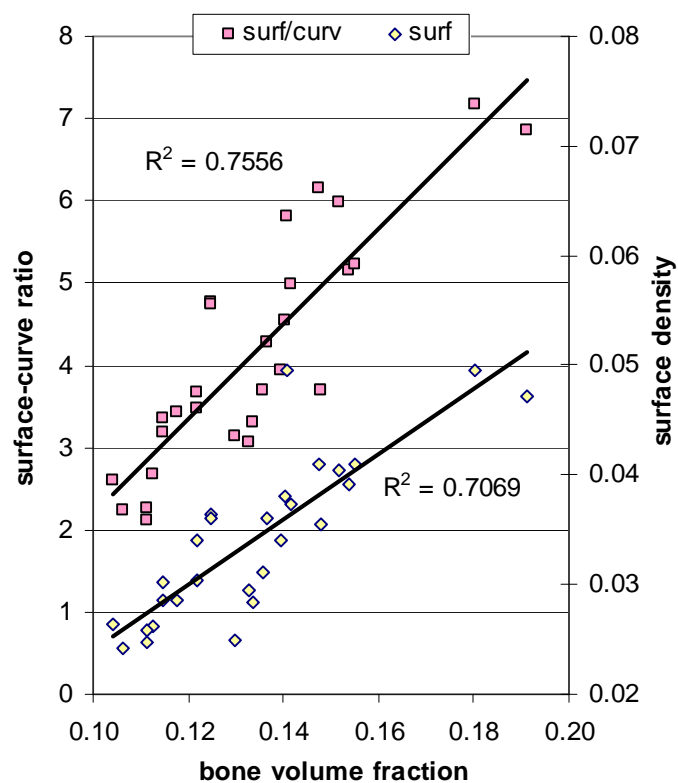

Figure 8: Surface densities (diamonds, right axis) and surface/curve ratios (squares, left axis) versus bone volume fraction for a cohort of subjects (n=28).